2014

High frequency normal mode statistics in a shallow water waveguide: The effect of random linear internal waves

Raghukumara, Kaustubha

High frequency normal mode statistics in a shallow water waveguide: The effect of random linear internal waves

Kaustubha Raghukumar[a] and John A. Colosi
Oceanography Department, Naval Postgraduate School, Monterey, California 93943

(Received 26 November 2013; revised 4 April 2014; accepted 16 May 2014)

Using transport theory and Monte Carlo numerical simulation, the statistical properties of mode propagation at a frequency of 1 kHz are studied in a shallow water environment with random sound-speed perturbations from linear internal waves. The environment is typical of summer conditions in the mid-Atlantic bight during the Shallow Water 2006 experiment. Observables of interest include the second and fourth moments of the mode amplitudes, which are relevant to full-field mean intensity and scintillation index. It is found that mode phase randomization has a strong adiabatic component while at the same time mode coupling rates are significant. As a consequence, a computationally efficient transport theory is presented, which models cross-mode correlation adiabatically, but accounts for mode coupling using the mode energy equations of Creamer [(**1996**). J. Acoust. Soc. Am. **99**, 2825–2838]. The theory also has closed-form expressions for the internal wave scattering matrix and a correction for an edge effect. The hybrid transport theory is shown to accurately reproduce many statistical quantities from the Monte Carlo simulations.
 [http://dx.doi.org/10.1121/1.4881926]

PACS number(s): 43.30.Bp, 43.30.Re, 43.60.Cg [TFD] Pages: 66–79

I. INTRODUCTION

The coastal ocean is an acoustically complex shallow water environment that is often subject to intensive internal and surface wave activity that lead to fluctuating acoustic fields (Katsnelson *et al.*, 2012). The statistical nature of random linear internal waves in the ocean is remarkably universal in a wide variety of deep and shallow water environments, and characterized by the parametric Garrett-Munk (GM) spectrum (Garrett and Munk, 1979). In this work, we focus on the statistical description of the acoustic scattering that can occur due to the ocean's random fields of internal gravity waves. Much of the work in this area has been directed at deep water environments where to a larger degree atmospheric and geologic effects are diminished, packets of intense non-linear waves are absent, and the random internal-wave field is well modeled by GM internal wave spectrum (Flatte *et al.*, 1979). While some earlier work examined random internal-wave effects in shallow-water environments (Creamer, 1996; Apel *et al.*, 1997), recent results using mode-transport theory (Colosi and Morozov, 2009; Colosi *et al.*, 2012b) appears to have put the scattering theory for both deep and shallow water environments on solid theoretical ground. The purpose of this study is to build upon the success of the aforementioned transport theory by examining higher acoustic frequencies in shallow water, where the large number of modes requires added efficiencies from analytic expressions and other physical approximations. While random surface gravity waves can also play an important role at high frequencies (Thorsos *et al.*, 2004), we reserve treatment of that subject for a companion paper.

Here we examine the predictability of acoustic fluctuations in shallow water at high frequencies (1000 Hz). The statistical quantities of interest in this paper are the mean and variance of acoustic intensity. We focus our attention on a transport theory for mode coupling induced by sound speed perturbations as a result of random linear internal waves described by a shallow water version of the GM spectrum. This paper should therefore be viewed as extending the work by Colosi *et al.* (2012b) to higher frequencies, applied to a non-canonical environment as was measured during Shallow Water 2006 (SW06). New closed-form expressions for the transport scattering matrix are proposed that lead to improved numerical tractability. It was found by Colosi *et al.* (2012b) that mode coherences in a shallow water environment have a strong adiabatic component, even in the presence of mode coupling. Consequently, a hybrid theory for mode coherences is proposed which combines mode energies as derived by Creamer (1996) with adiabatic phase terms. A new expression is also proposed that mitigates the "edge effect," as was detailed by Colosi *et al.* (2012b) The resulting hybrid transport theory with a correction for the edge effect shows good agreement with full-field Monte Carlo simulations. Mode coupling is shown to be strongly dependent on mode number, with internal waves preferentially coupling the lower order modes. Additionally, while mode energies readily show the effects of mode coupling, mode coherences remain strongly adiabatic. Both mode coupling and adiabatic phase randomization effects are shown to most strongly affect modes whose turning depths are in the thermocline. Fourth-moment statistics, namely the scintillation index (SI), is shown to further highlight the importance of mode coupling where improved agreement with Monte Carlo simulations is observed by the hybrid transport theory relative to adiabatic theory.

The organization of this paper is as follows. In Sec. II, we provide an overview of transport theory, and develop

[a]Author to whom correspondence should be addressed. Electronic mail: kraghuku@nps.edu

 0001-4966/2014/136(1)/66/14/$30.00

expressions for mode coherences based on new expressions for the scattering matrix, and treatment of the edge effect. Section III describes the modeled SW06 environment, along with computational methods employed in the Monte Carlo simulations, and transport theory calculations. Section IV contains results using the updated transport theory along with Monte Carlo simulations that validate transport theory results. Finally, Sec. V concludes the paper and analyses mode coupling and coherence effects in a high frequency regime.

II. TRANSPORT THEORY

This section begins with background material on the transport equation for the range evolution of the cross-mode coherence matrix. A hybrid transport theory is then presented, along with new equations for the scattering matrix, and treatment of the "edge" effect.

Using a two-dimensional normal mode-based approach, the acoustic pressure field, $p(r, z)$ can be expressed as

$$p(r,z) = \sum_{n=1}^{N} \frac{a_n(r)\phi_n(z)}{\sqrt{k_n r}}, \tag{1}$$

where N is the maximum acoustic mode number, $\phi_n(z)$ is the unperturbed mode shape, $l_n = k_n + i\alpha_n$ is the complex eigenwavenumber, and it is seen that all variability is contained in the range-dependent mode amplitude, $a_n(r)$. The effect of bottom attenuation on mode shape is neglected, following the perturbational approach of Jensen *et al.* (1994), where in the presence of weak attenuation, computational simplicity is achieved by using real mode shapes and complex wavenumbers.

Dozier (1982) and Creamer (1996) expressed the evolution equation for mode amplitudes in shallow water as

$$\frac{da_n}{dr} - il_n a_n = -i\sum_{m=1}^{N} \Gamma_{mn}(r) a_m(r), \tag{2}$$

where $\Gamma_{mn}(r)$ is the symmetric coupling matrix, which in the presence of internal wave-induced sound speed perturbations is given by

$$\Gamma_{mn}(r) = \frac{k_0^2}{\sqrt{k_n k_m}} \int_0^D \frac{\phi_n(z)\phi_m(z)}{\rho_0(z)} \frac{\delta c(r,z)}{c_0} dz, \tag{3}$$

where $\delta c(r, z)$ is the sound speed perturbation for a representative sound speed c_0, D is the water depth, $\rho_0(z)$ is the density profile, and $k_0 = \omega/c_0$ is a representative wavenumber at the acoustic frequency ω.

Transport theory provides expressions for the range evolution of various moments of intensity such as the first moment, $\langle I \rangle = \langle |p|^2 \rangle$, and second moment $\langle I^2 \rangle = \langle |p|^4 \rangle$. The mean intensity can be expressed as

$$\langle I(r,z) \rangle = \langle |p(r,z)|^2 \rangle = \sum_{n=1}^{N}\sum_{p=1}^{N} \frac{\langle a_n a_p^* \rangle (r)}{r} \frac{\phi_n(z)\phi_p(z)}{\sqrt{k_n k_p}}, \tag{4}$$

where $\langle a_n a_p^* \rangle (r)$ can be recognized as the cross-mode coherence matrix. Similarly, the mean square intensity can be expressed as

$$\langle I^2(r,z) \rangle = \sum_{n}\sum_{p}\sum_{m}\sum_{q} \frac{\langle a_n a_p^* a_m a_q^* \rangle}{r^2} \frac{\phi_n(z)\phi_p(z)\phi_m(z)\phi_q(z)}{\sqrt{k_n k_p k_m k_q}}, \tag{5}$$

where $\langle a_n a_p^* a_m a_q^* \rangle$ is the fourth-moment of mode amplitudes.

A useful measure of intensity fluctuations is the SI, given by

$$\mathrm{SI} = \langle I^2 \rangle / \langle I \rangle^2 - 1, \tag{6}$$

or alternatively the intensity variance $\langle I \rangle^2 - \langle I^2 \rangle$ gives the uncertainty in the mean intensity. Creamer (1996) first derived transport theory expressions for the range evolution of the cross-mode coherence matrix and the fourth-moment of mode amplitudes, but neglected the off-diagonal terms of the cross-mode coherence matrix in his asymptotic analysis of the SI. Colosi and Morozov (2009) re-derived Creamer's expression for the range evolution of the cross-mode coherence matrix and showed that the diagonal of the cross-mode coherence matrix [mode energies, Dozier and Tappert (1978a)] is roughly independent of the off-diagonal terms, thus explaining the excellent agreement with simulations observed by Dozier-Tappert's transport theory for mode energies. Of particular interest was their result that in a deep water environment both mode energies and cross-mode coherences decay in range at a similar rate, demonstrating the equivalence of mode coupling and adiabatic effects in mode phase randomization. However, in a more recent paper, Colosi *et al.* (2012b) applied transport theory to a shallow water environment typical of the SW06 experiment on the Mid-Atlantic bight (Lynch and Tang, 2008). At frequencies between 200 and 400 Hz, and over distances of tens of kilometers, a simple adiabatic theory was shown to sufficiently explain most of the propagation physics.

A. Hybrid theory

The full transport theory expression, as derived by Colosi and Morozov (2009), for the range evolution of the cross-mode coherence matrix, involves the computation of an internal wave scattering matrix (more below), the size of which can be intractable at high frequencies, where there are a large number of propagating modes. For N propagating modes, the size of the scattering matrix is $N^2 \times N^2$. At 1 kHz, the shallow water environment studied in this paper can support 53 propagating modes, resulting in a 2809×2809 scattering matrix. An approximate estimate of the number of propagating modes can be obtained using the mode cutoff expression for a Pekeris waveguide, $N = (k_0 D/\pi)\sin\left(\cos^{-1}(c_0/c_b)\right) + 0.5$, where c_b is the sound speed in the sea bottom. This gives values of $N = 12$ at 200 Hz, $N = 21$ at 400 Hz, $N = 81$ at 1500 Hz, and $N = 162$ at 3000 Hz, showing how the size of the scattering matrix becomes increasingly intractable at higher frequencies.

To surmount this problem, a hybrid approach is put forth where the adiabatic expression for the evolution of mode coherences [Eq. (28) in Colosi and Morozov (2009)] is adjusted for range evolution of mode amplitudes (i.e., mode coupling), to give

$$\langle a_n a_p^* \rangle(r) = \langle |a_n|^2 \rangle^{1/2}(r) \langle |a_p|^2 \rangle^{1/2}(r) e^{i\left(\theta_n(0)-\theta_p(0)\right)} \times e^{i(k_n-k_p)r} e^{-(I_{nn,nn}-2I_{nn,pp}+I_{pp,pp})r}. \quad (7)$$

Here, $\langle |a_n|^2 \rangle^{1/2}(r)$ are the range dependent mode amplitudes caused by mode coupling (more below), θ_n is the initial phase of the mode n (for a point source, θ_n is either 0 or π), and $I_{mn,qp}$ is the internal wave scattering matrix, given by

$$I_{mn,qp} = \int_0^\infty d\xi \Delta_{mn,qp}(\xi) e^{-ik_{qp}\xi}, \quad (8)$$

where $\Delta_{mn,qp}(\xi) = \langle \Gamma_{mn}(r) \Gamma_{qp}(r+\xi) \rangle$ is the correlation function of the symmetric mode coupling matrix [Eq. (3)] in the presence of internal waves, for range separation ξ. The acoustic mode wavenumber difference is $k_{qp} = k_p - k_q$. In general, $I_{mn,qp}$ is an $N^2 \times N^2$ matrix, but the hybrid approach only requires the calculation of an $N \times N$ scattering matrix, a considerable reduction in computational complexity. It should be noted that there is no requirement for the scattering matrix in Eq. (8) to be symmetric with respect to $mn \leftrightarrow qp$ exchange, even though the correlation of the mode coupling matrix, $\Delta_{mn,qp}(\xi)$ follows this symmetry. The exponential multiplier $e^{ik_{qp}\xi}$ in Eq. (8) breaks the symmetry. However, in the adiabatic approximation, $k_{qp} = 0$, so $I_{nn,pp}$ ends up being symmetric. Physically, this is consistent with the assumption made in the adiabatic approximation that there is no interaction between modes, and individual mode energy is conserved when the attenuation $\alpha_n = 0$.

The hybrid approach can be justified by first recognizing that the evolution of mode energies is insensitive to the off-diagonal coherence terms (Colosi and Morozov, 2009). As a result, mode energies in Eq. (7) can be obtained by solving Creamer's equation

$$\frac{d\langle |a_n|^2 \rangle}{dr} = -2\alpha_n \langle |a_n|^2 \rangle + \sum_{m=1}^{N} 2\mathrm{Re}(I_{mn,mn}) \left(\langle |a_m|^2 \rangle - \langle |a_n|^2 \rangle \right). \quad (9)$$

Next, the inclusion of the adiabatic phase terms in Eq. (7) can be justified by recognizing that the off-diagonal elements of the cross-mode coherence matrix were observed to have a strong adiabatic component in shallow water (Colosi *et al.*, 2012b), i.e., the phase randomization between propagating modes has a greater contribution from sound speed perturbations than from mode coupling.

Similarly, following the approach of Colosi *et al.* (2012b) who derived an adiabatic expression for the fourth moment of mode amplitudes, the hybrid transport theory expression for the fourth-moment is given by

$$\langle a_n a_p^* a_m a_q^* \rangle = \hat{a}_n \hat{a}_p^* \hat{a}_m \hat{a}_q^* \exp[-(I_{nn,nn} + I_{pp,pp} + I_{mm,mm} + I_{qq,qq} + 2[I_{nn,mm} + I_{pp,qq} - I_{nn,pp} - I_{nn,qq} - I_{mm,pp} - I_{mm,qq}])r], \quad (10)$$

where $\hat{a}_m = \langle |a_m|^2 \rangle^{1/2}(r) e^{ik_n r}$. Note that the attenuation term α_n is not contained in this equation because $\langle |a_m|^2 \rangle(r)$ has that factor included in Eq. (9).

The internal wave scattering matrix, $I_{mn,qp}$, is given by a new closed-form expression (see the Appendix for derivation),

$$I_{mn,qp} = \sum_{j=1}^{J} G_{mn}(j) G_{qp}(j) H(j) \frac{4a}{\pi |k_{qp}|} \left[\frac{\cos\theta_{min}}{(a^2+1)(a^2+2-a^2\cos 2\theta_{min})} \frac{\mathrm{atanh}\left(\sqrt{\frac{a^2}{a^2+1}} \cos\theta_{min} \right)}{2a(a^2+1)^{3/2}} + i \frac{\pi}{4a(a^2+1)^{3/2}} \right], \quad (11)$$

where J is the maximum internal wave mode number and

$$G_{mn}(j) = k_0^2 \sqrt{\frac{2}{k_n k_m}} \int_0^D dz \langle \mu^2(z) \rangle^{1/2} \times \sin[\pi j \hat{z}(z)] \frac{\phi_n(z)\phi_m(z)}{\rho_0(z)}. \quad (12)$$

Here $\langle \mu^2(z) \rangle$ is the fractional sound-speed variance, given by

$$\langle \mu^2(z) \rangle = \frac{\zeta_0^2}{c_0^2} \frac{N_0}{N(z)} \left(\frac{dc}{dz} \right)_p^2, \quad (13)$$

with $\zeta_0 = 2$ m being a reference displacement, $N_0 = 3$ cycles per hour a reference buoyancy frequency, $N(z)$ the

Brünt-Vaisala buoyancy frequency, and $(dc/dz)_p$ is the potential sound speed gradient. Next, $\hat{z}(z)$ is the Wentzel-Kramers-Brillouin (WKB) stretched vertical coordinate and $H(j) = N_j/(j^2 + j_*^2)$ is the GM vertical mode spectrum with N_j being the normalization factor and j_* the modal band width parameter. Other factors are $a = k_j/|k_{qp}|$ with $k_j = \pi fj/N_0 B$ the internal wave wavenumber, f the Coriolis frequency, and $N_0 B = \int_0^D N(z)dz$. Lastly, $\sin\theta_{\min} = |k_{qp}|\, f/(k_j N_{\max})$, with $N_{\max}$ the maximum buoyancy frequency. For the special case of $k_{qp} = 0$, the terms following $H(j)$ in Eq. (11) simplify to $(2/\pi)(1/k_j)(k_{\max}^2/k_{\max}^2 + k_j^2)$, where $k_{\max}$ is the maximum horizontal wavenumber (see the Appendix), and the resulting adiabatic scattering matrix can be written as

$$I_{nn,pp} = \sum_{j=1}^{J} G_{nn}(j) G_{pp}(j) H(j) \frac{2}{\pi} \frac{1}{k_j} \frac{k_{\max}^2}{k_{\max}^2 + k_j^2}. \tag{14}$$

B. Edge effect

Inherent to the transport theory explained thus far is the assumption that the range r is longer than the correlation length of internal waves. The correlation length for internal waves, approximately given by $\sum_{j=1}^{J} H(j)/k_j$ (Colosi *et al.*, 2012b), is 3.6 km for the environment considered here. This assumption results in an overcounting of scattering effects which leads to mode coherences that decay faster than they should at short ranges. We next discuss an analytical correction to the overcounting from the edge effect [Colosi *et al.*, 2012b, Eq. (18)[1]].

In the hybrid equation for mode coherence [Eq. (7)], the term in the last exponential $[(I_{nn,nn} - 2I_{nn,pp} + I_{pp,pp})r = A_{np}(r)]$ can be written using adiabatic theory, as (Colosi and Morozov, 2009)

$$A_{np}(r) = \frac{1}{2}\int_0^r dr_1 \int_0^r dr_2 \left(\Delta_{nn,nn}(|\xi|) + \Delta_{pp,pp}|\xi|) - 2\Delta_{nn,pp}|\xi|\right), \tag{15}$$

where $\xi = r_1 - r_2$. Changing the variable of integration in the inner integral of Eq. (15) to ξ gives

$$A_{np}(r) = \frac{1}{2}\int_0^r dr_1 \int_{r_1 - r}^{r_1} d\xi \left(\Delta_{nn,nn}(|\xi|) + \Delta_{pp,pp}|\xi|) - 2\Delta_{nn,pp}|\xi|\right). \tag{16}$$

The assumption that r is much larger than the correlation length of internal waves allows us to take the ξ-integral limits from $-\infty$ to ∞ giving

$$A_{np}(r) \simeq \frac{1}{2}\int_0^r dr_1 \int_{-\infty}^{\infty} dr_2 \left(\Delta_{nn,nn}(|\xi|) + \Delta_{pp,pp}|\xi|) - 2\Delta_{nn,pp}|\xi|\right). \tag{17}$$

For range separations larger than the correlation length of $\Delta_{nn,pp}|\xi|$, there are no consequences in taking the integral limits to $\pm\infty$, since this substitution essentially counts zeros. However, at shorter separations, Eq. (17) overcounts, even though it is consistent with transport theory. This overcounting, termed the edge effect by Colosi *et al.* (2012b), and is overcome by evaluating $A_{np}(r)$ using Eq. (15) instead of Eq. (17).

While Eq. (15) can be numerically evaluated for a GM spectrum, an approximate closed-form solution is sought by first recognizing that the correlation function for the mode coupling matrix, $\Delta_{nn,pp}(|\xi|)$, is more easily obtained for a Lorentzian internal wave spectrum than the GM spectrum. For the GM-equivalent Lorentzian spectrum (Colosi and Morozov, 2009),

$$\Delta_{nn,pp}(|\xi|) = \sum_{j=1}^{J} H(j) G_{nn}(j) G_{pp}(j) \exp\left(-\hat{k}_j|\xi|\right). \tag{18}$$

This yields

$$A_{np}(r) = \sum_{j=1}^{J} H(j) \frac{\left(G_{nn}(j) - G_{pp}(j)\right)^2}{\hat{k}_j} \left(r + \frac{\exp\left(-\hat{k}_j r\right) - 1}{\hat{k}_j}\right), \tag{19}$$

where $\hat{k}_j = \sqrt{2}k_j$. It was verified that $A_{np}(r)$, when numerically evaluated for the GM spectrum, is very similar to the closed-form expression, Eq. (19) for the equivalent Lorentzian spectrum.

A similar edge-correction can be obtained for the exponential terms in the fourth moment of mode amplitudes, Eq. (10),

$$B_{np,mq}(r) = (I_{nn,nn} + I_{pp,pp} + I_{mm,mm} + I_{qq,qq} + 2[I_{nn,mm} + I_{pp,qq} - I_{nn,pp} - I_{nn,qq} - I_{mm,pp} - I_{mm,qq}])r$$
$$= \sum_{j=1}^{J} H(j) \frac{\left(G_{nn}(j) - G_{pp}(j) + G_{mm}(j)\right)^2}{\hat{k}_j} \left(r + \frac{\exp\left(-\hat{k}_j r\right) - 1}{\hat{k}_j} \right). \quad (20)$$

Mode coherences and mode amplitude fourth moments, for the hybrid transport theory with a correction for the edge effect, can therefore be calculated using Eqs. (7) and (10), with $A_{np}(r)$ given by Eq. (19), $B_{np,mq}$ given by Eq. (20), and $G_{mn}(j)$ by Eq. (12).

III. NUMERICAL COMPUTATIONS FOR THE SW06 ENVIRONMENT

This section briefly describes details of the acoustic propagation environment as measured during the SW06 experiment, conducted off the New Jersey continental shelf, and upon which numerical simulations in this paper are based. Further details of the experiment and the acoustic fluctuations observed may be found in the papers by Lynch and Tang (2008) and Colosi *et al.* (2012a). Also described are the Monte Carlo simulations and the numerical implementation of the transport equations for mode coherence.

Figure 1 shows the background sound-speed and buoyancy frequency profile obtained by averaging 15 conductivity-temperature-depth (CTD) casts made during SW06. Environmental and acoustic sensors during SW06 were deployed along a T-shaped pattern (Tang *et al.*, 2007), with one arm of the "T" traversing the cross-shelf direction, and the other traversing an along-shelf direction. The CTD casts were taken in the vicinity of the center of the T-shaped pattern, in 86 m deep water, within 8.5 km of the SW30 mooring (Colosi *et al.*, 2012a). Also shown in Fig. 1 are a subset of the 1000 Hz vertical acoustic modes $[\phi_n(z)]$ computed using this sound speed profile, and the root mean square (rms) sound speed fluctuation $[\langle \mu^2(z) \rangle^{1/2}]$ used in the GM internal wave model (further details below), as modeled using the method of Colosi and Brown (1998). The presence of a sound-speed minimum at a 25 m depth leads to the trapping of lower-order modes in this mid-water region. This has implications for the mode number dependence of mode coupling and mode phase randomization, a subject explored in Secs. IV and V. This sound-speed minimum at 25 m also results in a change in sign of the potential sound speed gradient, resulting in the null in the rms sound speed fluctuation. A lowering of sound-speed is also seen toward the surface, leading to enhanced acoustic interaction with the surface, a subject explored in a companion paper.

Monte Carlo simulations are conducted by repeatedly solving the coupled mode equation [Eq. (2)] using the eigenvector technique of Dozier and Tappert (1978b), over 256

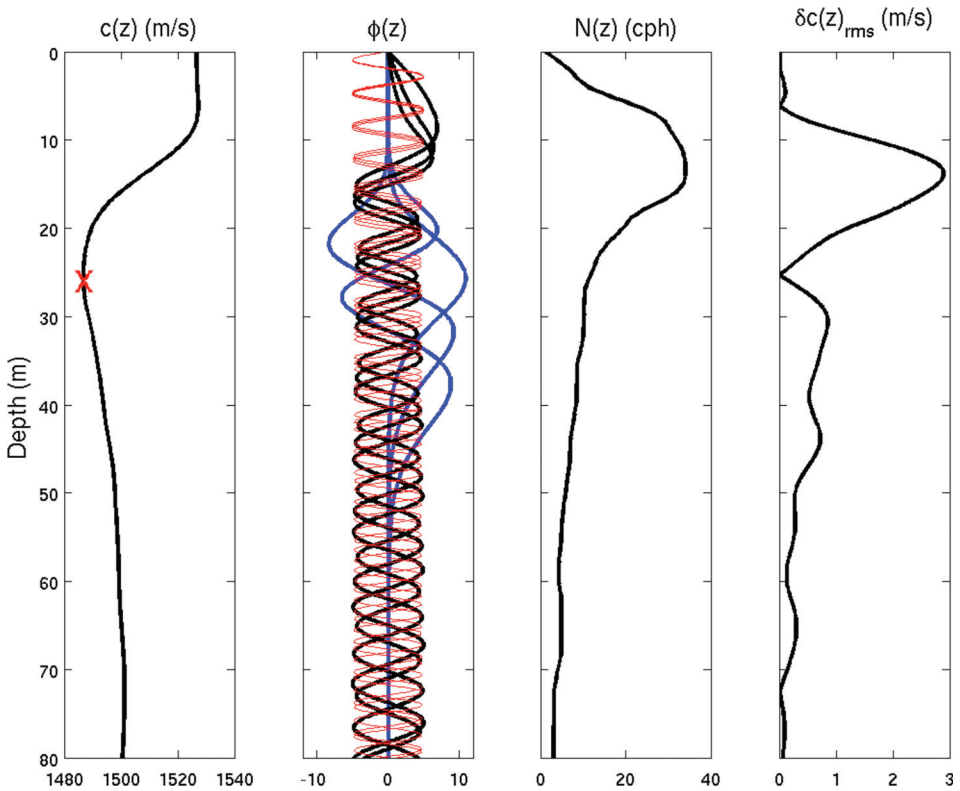

FIG. 1. SW06 background sound speed profile along with source location, acoustic modes 1-3 (blue line), 18-21 (black line), 51-53 (red line), buoyancy frequency, and the modeled rms sound speed fluctuation.

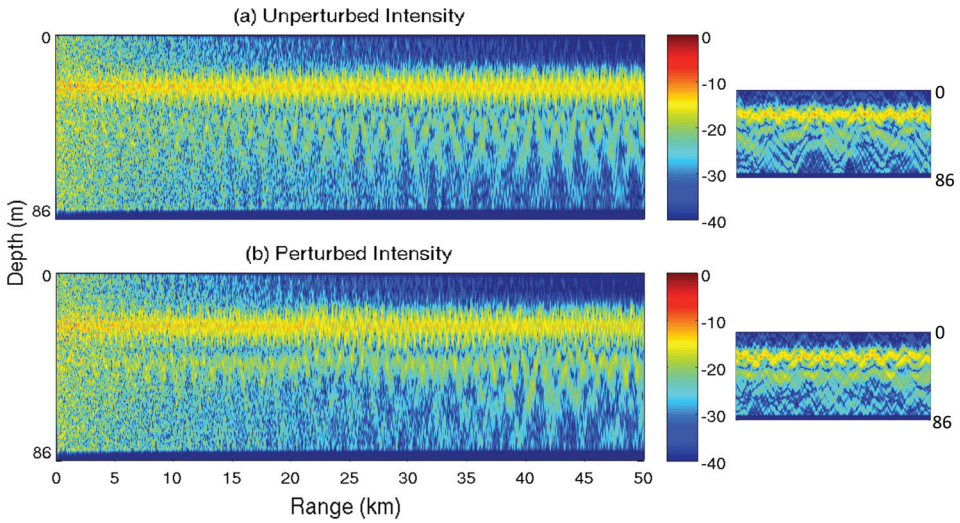

FIG. 2. An example showing the normalized acoustic intensity (dB re 1 μPa), (a) with no sound speed fluctuations, and (b) with a perturbed sound speed field. The insets show the respective intensities between 30 km and 35 km.

realizations of the internal wave field. Horizontal scales of modeled internal waves range from 20 m to 100 km. A point source is located at a depth of 25 m, which is the depth of the sound speed minimum. The range evolution of mode energies and coherences is calculated out to 50 km, using a 5 m range step. Attenuation is included in the calculations, both in the sea bottom, with an attenuation constant of $\alpha^{\lambda} = 0.2\,\mathrm{dB}/\lambda$, and in the water column as a result of boric acid relaxation and magnesium sulfate relaxation (Munk *et al.*, 1995). The density of the water column and sea bottom is fixed at $1000\,\mathrm{kg/m^3}$ and $1500\,\mathrm{kg/m^3}$, respectively. Sound speed in the bottom is fixed at 1700 m/s. All other parameters of the acoustic waveguide and internal wave model were chosen to be exactly the same as in Colosi *et al.* (2012b), who obtained the values based on a detailed analysis of the SW06 internal wave environment (Colosi *et al.*, 2012a).

Figure 2 shows an example of 50 km range acoustic propagation of a 1000 Hz signal in this shallow water environment. Shown are the unperturbed and perturbed intensities for a single realization of the internal-wave field. The intensities are normalized by the maximum unperturbed intensity. The inset shows the intensities over a 5 km region between 30 km and 35 km. Cylindrical spreading has been omitted in the calculations of acoustic intensity. The plots of unperturbed and perturbed intensity show that the effect of higher mode stripping by interaction with the sea bottom gives rise to an interference pattern dominated by lower modes at longer ranges. The 5 km detail shows more clearly the effect of mode coupling, where an acoustic shadow zone close to the bottom at a 32 km range is now insonified as a result of lower modes coupling into higher modes.

Now on the matter of transport theory, the calculations for the mode coherence are made by computing the hybrid mode coherence [Eq. (7)], with mode energies obtained by solving Creamer's energy equation [Eq. (9)]. The mode energy equation is numerically solved at each range step using a variable-order Adams-Bashforth-Moulton method, with the scattering matrices given by the new analytical expression, Eq. (11). The adiabatic scattering matrices in the hybrid coherence equation [Eq. (7)] are computed either without the correction for the edge effect [Eq. (14)], or with the appropriate edge correction [Eq. (19)]. The hybrid transport theory was found to compute mode coherences almost 3000 times faster than the full coherence calculation, in addition to the considerably improved numerical tractability of the scattering matrix. Mode amplitude fourth moments are calculated using Eq. (10), with the edge correction given by Eq. (20).

IV. RESULTS

Various aspects of the transport theory that predicts the evolution of mode energies, cross-mode coherences, mean intensity, and SI in the presence of random linear internal waves are demonstrated here in the SW06 environment. Monte Carlo simulations of acoustic propagation through a sound speed field perturbed by internal waves are employed to validate transport theory results.

A. Mode coupling and phase randomization

The relative strengths of internal wave-induced mode coupling and mode phase randomization are studied in this section, as a precursor to presenting the mode energies and coherences. The mode number dependence of coupling and adiabatic phase randomization is examined, and a useful metric is proposed that measures the strength of nearest-neighbor mode coupling.

1. Attenuation and mode coupling

It is important to know the relative rates of coupling and attenuation in order to understand the competing effects of either phenomena, i.e., whether modes are coupled before they are attenuated, or vice versa. To look at coupling, we examine Dozier-Tappert's mode energy equation [Eq. (9) with attenuation set to zero] which can be written in the matrix form $d\mathbf{A}/d\mathbf{r} = \mathbf{F}^T\mathbf{A}$, where $\mathbf{A} = \left[\langle|a_1|^2\rangle \;\; \langle|a_2|^2\rangle \cdots \langle|a_N|^2\rangle\right]^T$ is a $N \times 1$ vector of mode energies, and $\mathbf{F}$ is a $N \times N$ matrix with elements $F_{mn} = 2\mathrm{Re}\{I_{mn,mn}\}$ if $m \neq n$, and $F_{nn} = 2\mathrm{Re}\{I_{nn,nn}\} - \sum_{m=1}^{N} 2\mathrm{Re}\{I_{mn,mn}\}$. The solution to this equation can be expressed as $\mathbf{A}(r) = \mathbf{V}\,\exp(\mathbf{D}r)\mathbf{V}^T\,\mathbf{A}^0$ where

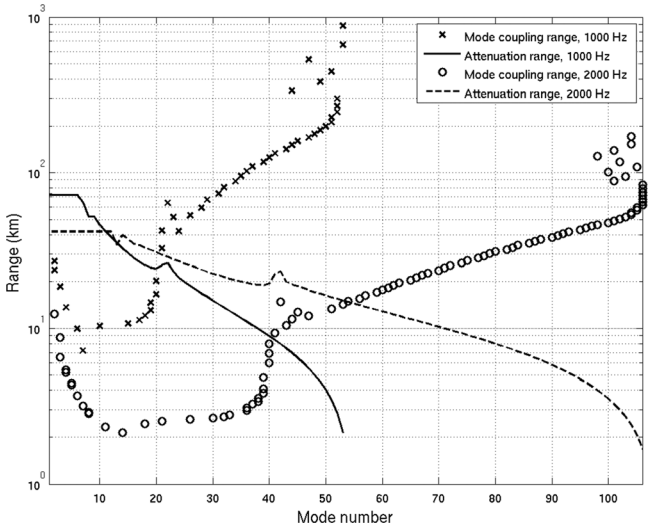

FIG. 3. Mode coupling and attenuation ranges (km) in the presence of internal waves, at 1000 Hz (solid and ×) and 2000 Hz (dashed and ○). Note that the attenuation is constant for low modes that are only subject to water column attenuation and no bottom interaction/attenuation.

$\mathbf{V}$ is a matrix whose columns are the eigenvectors of $\mathbf{F}^T$ and $\mathbf{D} = \mathrm{diag}[\lambda_1,\ldots,\lambda_N]$, where λ_n are the eigenvalues of $\mathbf{F}^T$. In this analysis, we do not seek a solution to Eq. (9) using the above matrix diagonalization, but focus attention on the eigenvalues of $\mathbf{F}^T$. The eigenvalues represent the exponential decay rate in eigenspace of the initial mode energies A_n^0. If individual eigenvectors are dominated by single modes, as they were found to be for the current propagation scenario, then the eigenvalues now directly represent energy decay rates by mode coupling for the dominating modes. The inverse of the eigenvalues, $R_n = \lambda_n^{-1}$, defined as the mode coupling range, therefore represents the e-folding range over which the relevant mode has experienced significant coupling. Given a mode coupling range, R_n, the dominating mode number is given by the index of the largest value in the corresponding eigenvector. Similarly, we also define the mode attenuation range, or the e-folding range over which a mode undergoes significant attenuation, as $P_n = [2\alpha_n]^{-1}$.

Figure 3 shows the mode coupling range, R_n, overlaid with the mode attenuation range, P_n, at 1000 Hz and 2000 Hz frequencies. At both frequencies, the mode coupling range generally increases with increasing mode number, implying that higher modes can propagate greater distances before they experience mode coupling. However, the effect of attenuation is such that higher modes begin to attenuate at significantly shorter ranges than the lower modes. This results in a competition between mode coupling and mode stripping by attenuation. Low modes that do not interact with the sea bottom have a constant attenuation range as a result of water column attenuation alone. The effect of increasing frequency is that a larger number of modes can undergo mode coupling before attenuation effects dominate. At 1000 Hz, this transition region is in the vicinity of mode 20, while at 2000 Hz the transition region is closer to mode 55. The combined effect, therefore, is that under the present fluctuation scenario, lower modes couple exclusively, and propagate with considerably lower attenuation than the higher modes.

2. Strength of mode coupling

A metric that shows the strength of mode coupling can be obtained by further examining the mode energy equation, Eq. (9). The matrix $\mathrm{Re}(I_{mn,mn})$ is strongly peaked along the diagonal leading to a strong interaction between neighbor modes. The dominance of nearest neighbor coupling comes from the assumption of small-angle scattering, since a coupling event between modes n and m represents a change in vertical angle. Small angle scattering is a consequence of the weak sound speed perturbations from linear internal waves. For the given perturbation scenario, an examination of the matrix $\mathrm{Re}(I_{mn,mn})$ confirmed that the off-diagonal elements of $\mathrm{Re}(I_{mn,mn})$ indeed decay rapidly away from the diagonal. Of course, in the full and hybrid transport theories we treat all neighbor interactions. The first off-diagonal element of $\mathrm{Re}(I_{mn,mn})$ is therefore a measure of nearest-neighbor mode coupling (i.e., strength of mode $m-1$ coupling into mode m). The dominance of nearest-neighbor mode coupling has been experimentally observed in deep water where modes with low initial energy can gain substantial energy via mode coupling if a neighboring mode has a high initial energy (Chandrayadula *et al.*, 2013). Under this assumption, the mode energy equation can be written as

$$\frac{d\langle|a_n|^2\rangle}{dr} = -2\alpha_n\langle|a_n|^2\rangle + D_n\left[\langle|a_{n-1}|^2\rangle - 2\langle|a_n|^2\rangle + \langle|a_{n+1}|^2\rangle\right], \tag{21}$$

where $D_n = 2\mathrm{Re}(I_{(n-1)n,(n-1)n})$ and it is assumed that $\mathrm{Re}(I_{(n-1)n,(n-1)n}) \simeq \mathrm{Re}(I_{n(n+1),n(n+1)})$. The quantity in the square brackets of Eq. (21) can be recognized as the discrete form of the second derivative. This equation can therefore be recognized as being of a similar form to a diffusion equation, where the diffusion constants D_n facilitate energy transfer from mode $n-1$ to mode n, and the rate of energy transfer depends on the mode energy difference, $\langle|a_{n-1}|^2\rangle - \langle|a_n|^2\rangle$. The diffusion constants, D_n, therefore indicate the strength of nearest neighbor mode coupling, and are plotted in Fig. 4 which shows the logarithm of the strength of nearest neighbor mode coupling as a function of mode number, at frequencies of 1000 Hz and 2000 Hz.

Internal waves are predicted to most strongly couple modes 1–20 at 1000 Hz and modes 1–40 at 2000 Hz, with higher modes being coupled with substantially lower strength. Internal wave induced sound speed perturbations have the largest amplitude displacements near the thermocline, located a depth of 16 m (Fig. 1), which is also the region in the water column where lower order acoustic modes have their upper turning depth.

Figure 5 shows the mode upper turning depth for all propagating acoustic modes at 1000 Hz and 2000 Hz. Modes that have their turning depth between 10 m and 20 m are seen to undergo the strongest coupling. Higher surface-interacting acoustic modes occupy the entire water column, and have turning depths outside the region of large sound speed perturbations. Consequently, the strength of mode coupling is substantially weaker than for lower acoustic

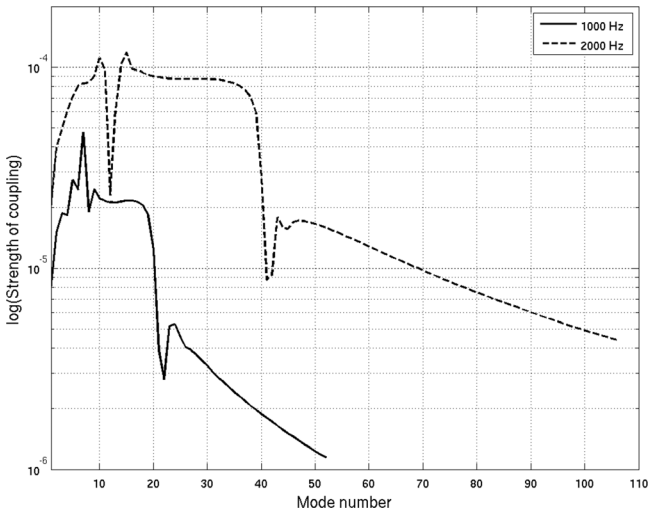

FIG. 4. Strength of nearest neighbor mode coupling (m^{-1}) in the presence of internal waves, at 1000 Hz (solid line) and 2000 Hz (dashed line).

modes. Modes 6 (1000 Hz) and 12 (2000 Hz) have their upper turning depth exactly at 16 m, the depth of largest mean sound speed perturbation. The peak (1000 Hz) or notch (2000 Hz) in mode coupling strength for these modes arises largely from the WKB mode summation in the function $\sum_{j=1}^{J} G^2_{m-1,m}(j)$ that results in a peak or notch at 16 m.

3. Phase randomization

In addition to mode coupling, sound speed fluctuations by random linear internal waves induce adiabatic phase randomization. Each propagating mode can be thought of as being randomly advanced or delayed by sound speed perturbations, with a resulting loss of cross-mode coherence. The phase randomization (or decorrelation) range for a mode pair ($R_{n,p}$) predicted by adiabatic theory, can be defined from Eq. (7) as $R_{n,p} = 1/(I_{nn,nn} - 2I_{nn,pp} + I_{pp,pp})$.

Figure 6 shows the adiabatic phase randomization range as a function of the mean mode upper turning depth for pairs

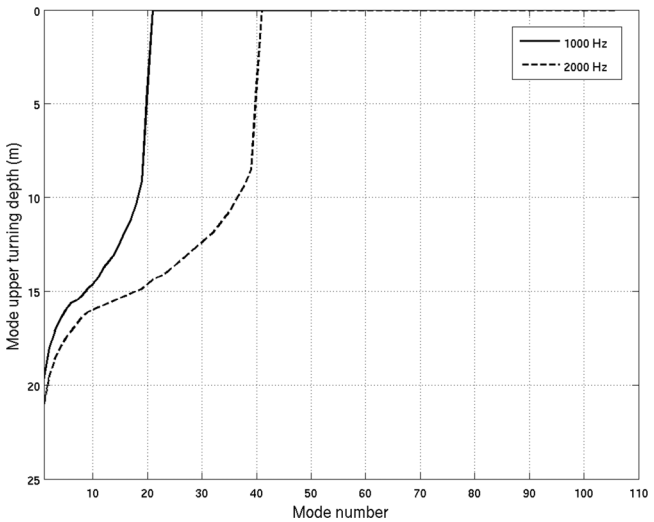

FIG. 5. Mode upper turning depth as a function of mode number, at 1000 Hz (solid line) and 2000 Hz (dashed line). For frequencies at 1000/2000 Hz, mode numbers greater than 21/41 have turning depths at $z = 0$ m.

of neighboring modes, at 1000 Hz and 2000 Hz. In general, the phase randomization range is seen to increase by 2 orders of magnitude as the mode turning depth goes from 20 m to 10 m, once again emphasizing the increasing phase randomization distances for the modes with turning depths outside the thermocline region. Modes that have their upper turning depth at the surface have adiabatic phase randomization ranges that further increase by several orders of magnitude to almost 10^5 km, indicating that these high modes can be expected to perfectly preserve their cross-mode coherence for the range separations studied in this paper.

Similar to Fig. 4, a peak (1000 Hz) and a notch (2000 Hz) in phase randomization range is observed for mode pairs with turning depths exactly at the depth of largest sound speed perturbations, due to the structure of the function $\sum_{j=1}^{J}\left(G_{nn}(j) - G_{pp}(j)\right)^2$. The mode phase randomization result, taken together with the fact that mode coupling ranges are extremely large for higher modes indicate that mode energies and coherences are largely preserved for higher modes from mode coupling and adiabatic effects, respectively. However, given the larger sub-bottom attenuation for high modes, the effect of the preserved coherence on observables such as mean intensity is expected to be negligible.

B. Mode energies

The competing effects of mode coupling and attenuation was demonstrated in Sec. IV A 1 by examining the mode coupling and attenuation ranges, along with a useful metric for nearest neighbor mode coupling. Here, Monte Carlo simulations of the range evolution of mode energies are compared with hybrid transport theory results.

Figure 7 shows mean mode energies for three sets of low, medium, and high modes. Shown are modes 1–3, 18–20, and 51–53. Mode energies have been scaled by $e^{+2\alpha_n r}$ to remove the effects of attenuation and to focus on mode coupling. Mode energies from the hybrid transport theory [dashed line, Eq. (9)] are overlaid by the Monte Carlo simulations (solid line). The non-adiabaticity of modal propagation is readily apparent for the lower modes where mode energies for both the Monte Carlo simulations and transport theory exhibit a drive toward equipartition of mode energies. This behavior is considerably different from that at 400 Hz (Colosi *et al.*, 2012b), where only weak coupling effects were observed, with the departure from adiabatic theory occurring only at a distance of 25 km from the source. Modes 18–20 are observed to reach local equipartition of energies at the 50 km range, while modes 51–53 undergo negligible mode coupling with mode energies that remain strongly adiabatic. Coupling-induced modal energy exchange is seen to decrease with increasing mode number, a result consistent with Fig. 4.

C. Mode coherences

The loss of coherence of lower modes was studied in Sec. IV. A by examining the adiabatic phase randomization range as a function of mode upper turning depth at 1000 Hz and 2000 Hz. Modes with upper turning depths in the thermocline region were seen to exhibit a loss of coherence over

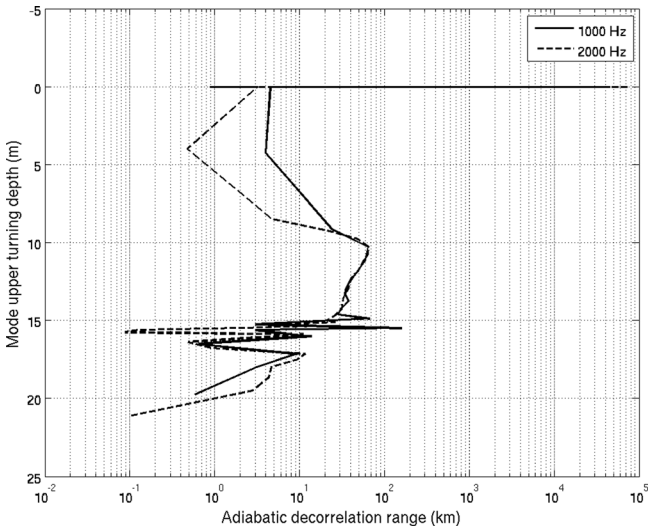

FIG. 6. Mode adiabatic decorrelation range (km) as a function of mode upper turning depth (m) at 1000 Hz (solid line) and 2000 Hz (dashed line).

distances of less than 1 km at kilohertz frequencies. Here, the range evolution of mode coherences computed using Monte Carlo simulations are shown to be in good agreement with transport theory results.

The range evolution of mode coherences is shown in Fig. 8 for three sets of mode pairs (lower modes 1–2, 3–4, 4–5, modes 19–20, 21–22, 23–24, and high modes 48–49, 50–51, and 52–53). Shown are the normalized mode coherences [i.e., $|\langle a_n a_p^* \rangle|(r)/\sqrt{\langle |a_n|^2 \rangle (r) \langle |a_p|^2 \rangle (r)}$] using the hybrid transport theory with the correction for the edge effect (dashed line) and Monte Carlo simulations (solid line). Also shown is the edge-uncorrected mode coherence for the lowest pairs of modes (dashed-dotted line). From Eq. (7), it can be seen that the normalization leaves only the adiabatic exponential terms intact, and the coherences shown are essentially those using the adiabatic transport theory, with and without the correction for the edge effect.

The overcounting of phase terms (edge effect), is readily apparent in the plots showing the hybrid transport theory. The correct treatment of this important effect results in a significantly better agreement with Monte Carlo simulations, similar to the improvements observed by Colosi *et al.* (2012b). The excellent agreement with Monte Carlo simulations suggest that mode coherences for the particular propagation scenario are adequately modeled using the edge-corrected adiabatic theory with the cross-mode coherences showing a strong mode number dependence, observed both in the Monte Carlo simulations (Fig. 8) and via the adiabatic phase randomization range (Fig. 6). A good agreement is seen between the decorrelation ranges predicted by Eq. (7) (and shown in Fig. 6) and those observed in Fig. 8, with the general result that the surface-interacting higher mode pairs exhibit increasing decorrelation ranges.

The combined results from Figs. 7 and 8 shows that coupling effects are stronger on the diagonal of the cross-mode coherence matrix (mode energies) than the off-diagonal terms (cross-mode coherence). It can be reasonably concluded that the loss of coherence by phase randomization is dominated by the effect of sound speed perturbations adiabatically advancing and delaying the propagating acoustic field (adiabatic effect), while the evolution of mode energies is dominated by mode coupling (non-adiabatic effect) and attenuation.

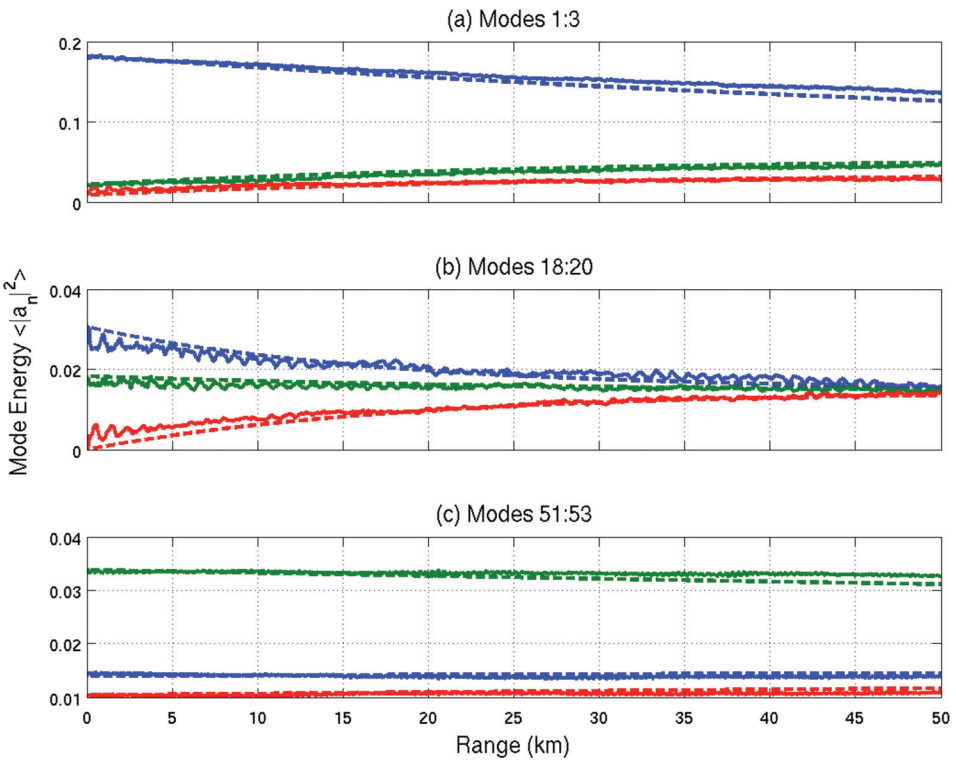

FIG. 7. Mode energies scaled to remove attenuation effects in order to focus on coupling effects, for (a): Modes 1–3 (blue, green, and red lines, respectively), (b): Modes 18–20, (c): Modes 51–53. Hybrid transport theory is the dashed line and Monte Carlo simulation is the solid line.

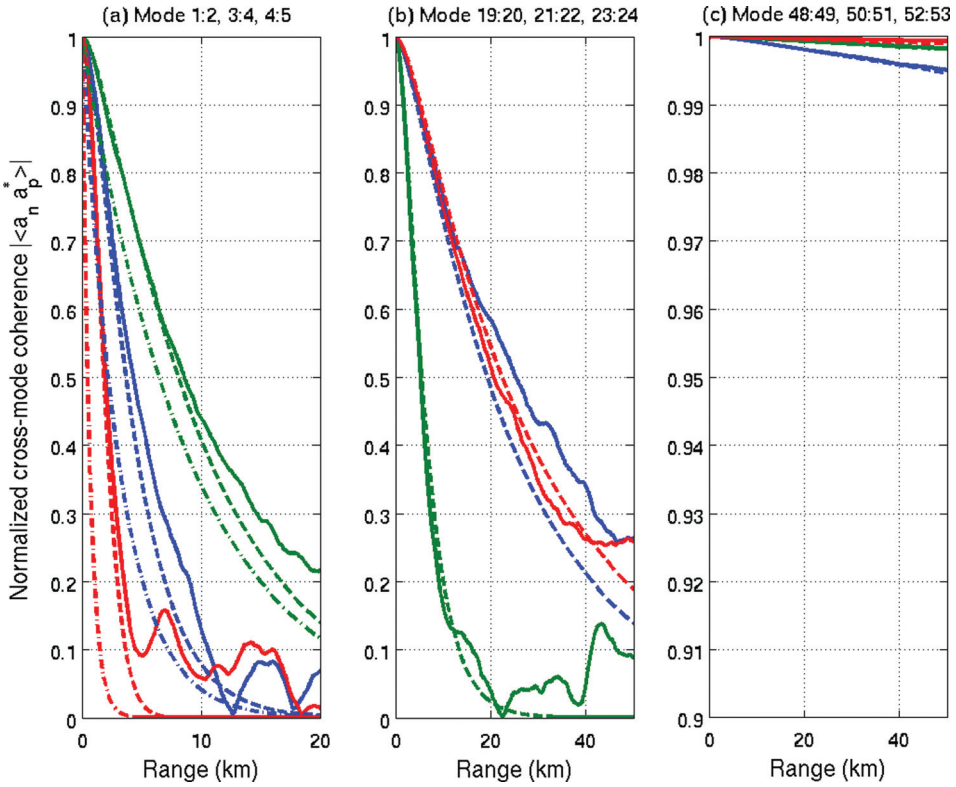

FIG. 8. Mode coherences for (a) mode 1 with 2 (blue line), mode 3 with 4 (green line), and mode 4 with 5 (red line), (b) mode 19 with 20 (blue line), mode 21 with 22 (green line), and mode 23 with 24 (red line), and (c) mode 48 with 49 (blue line), mode 50 with 51 (green line), and mode 52 with 53 (red line). Monte Carlo simulations are shown as the solid line, hybrid transport theory with edge correction is shown as the dashed line, and hybrid transport theory without edge effect correction is shown as the dashed-dotted line.

D. Mean intensity

Figure 9 shows the acoustic observable of mean intensity in decibels for a receiver located at a depth of 50 m, calculated using the hybrid transport theory (black line) overlaid with the unperturbed intensity (blue line) and Monte Carlo simulation (red line). Also shown are the mean intensities between 0 and 3.2 km, the approximate correlation length for internal waves as modeled in this particular shallow water environment.

The hybrid transport theory with the edge correction shows good agreement with the Monte Carlo simulations. The significance of the loss of coherence of lower propagating modes and mode stripping of higher modes by sea

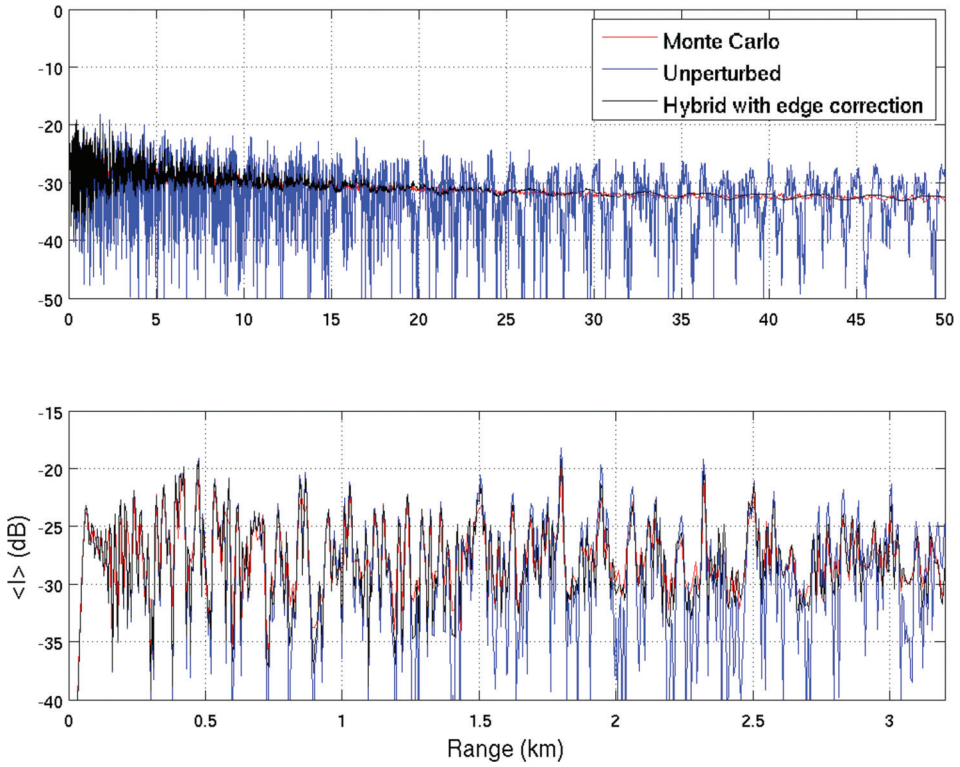

FIG. 9. Mean intensity (dB) for a receiver at a depth of 50 m, using transport theory without edge correction (blue line), with edge correction (black line), and Monte Carlo simulation (red line). The bottom panel shows an expanded view over 3.2 km.

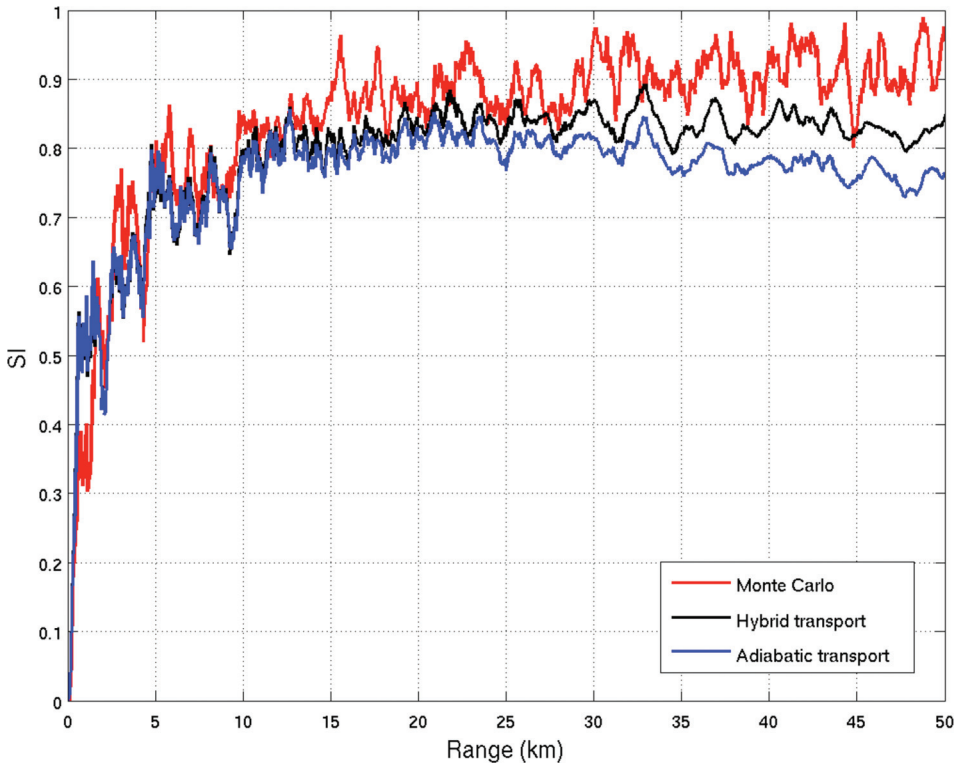

FIG. 10. Range evolution of the SI at 50 m depth at 1000 Hz. The red line shows the Monte Carlo simulation, the black line is the hybrid transport theory, and the blue line shows adiabatic transport theory.

bottom attenuation is clearly visible when contrasted with the unperturbed intensity, with the mean intensity showing an increasingly flat curve, devoid of any interference pattern.

E. Scintillation index

The range evolution of the SI, calculated using Eq. (6), is shown in Fig. 10 for a receiver at 50 m depth. A moving average filter over 500 m is applied to improve clarity and reduce fluctuations. Monte Carlo simulations (red line) are overlaid with hybrid (black line) and adiabatic transport theories (red line). The progressions of the various approaches to calculate mode coherence are readily apparent in the SI calculation. While the adiabatic transport theory shows reasonable agreement with the Monte Carlo simulations at short ranges, discrepancies are observed to increase with range. Inclusion of mode coupling effects (hybrid theory) is seen to reduce the discrepancy with full-field Monte Carlo simulations. However, the absence of phase terms from mode coupling in the hybrid approach prevents further agreement with Monte Carlo simulations. The SI at 1000 Hz is considerably different from that observed at 400 Hz in a similar shallow water environment by Colosi *et al.* (2012b). At short ranges (0 to 10 km), the SI at 400 Hz was seen to have frequent excursions above a value of 2, caused by fade-outs in mean intensity, with a final value close to 0.3 at a 50 km range. In contrast, the SI at 1000 Hz monotonically asymptotes without any significant excursions towards a value close to 1 at a 20 km range. From Colosi and Baggeroer (2004), the SI can be expressed as

$$\mathrm{SI} = 1 + \frac{1}{N}\left(\frac{\langle a^4\rangle}{\langle a^2\rangle^2} - 2\right), \tag{22}$$

where N is the number of acoustic modes, and $\langle a^2\rangle$, $\langle a^4\rangle$ are the second- and fourth-moments of mode amplitudes, respectively. At 400 Hz, the effective N is lower than at 1000 Hz due to greater mode stripping by sub-bottom attenuation, resulting in an SI far from 1. On the other hand, the larger effective N at 1000 Hz results in an SI closer to 1, indicative of a nearly saturated acoustic field.

V. DISCUSSION AND CONCLUSION

An efficient reduced-physics transport theory framework for high frequency acoustic propagation in shallow water was demonstrated in an environment typical of summer conditions in the mid-Atlantic bight, as measured during the SW06 experiment off the continental shelf of New Jersey.

New closed-form expressions have been proposed for the scattering matrix when random linear internal waves are described by the GM spectrum. A hybrid form of the transport theory was put forth where mode energies from Dozier-Tappert/Creamer's approach were used along with adiabatic phase terms to calculate the cross-mode coherence matrix. The validity of this approximation was based on the strong adiabatic component of mode coherences that was observed in SW06 propagation by Colosi *et al.* (2012b) and confirmed in this paper. Corrections to the hybrid theory were then developed in order to more accurately model phase terms at short ranges where the correlation length of internal waves is no longer greater than the range of interest. Analytical treatment of this edge effect was included in the hybrid transport theory for mode amplitude second- and fourth-moments. The new transport theory results for mode energies, coherences and mean intensity at 1000 Hz were confirmed to have an excellent agreement with Monte Carlo simulations. Regarding SI, while the hybrid transport theory showed

better agreement than adiabatic theory with Monte Carlo simulations, the absence of phase terms from mode coupling prevented a more complete agreement.

The mode number dependence of mode coupling phenomena was demonstrated at 1000 Hz and 2000 Hz via the competing effects of mode coupling and attenuation ranges. At both frequencies, low propagating modes were seen to have a smaller coupling range than the attenuation range, allowing for mode coupling effects to take precedence over attenuation effects. Higher propagating modes were seen to have smaller attenuation ranges as a result of greater sub-bottom and water column attenuation. This results in their being stripped before mode coupling reflects can occur. A metric to measure the strength of mode coupling was demonstrated by recognizing that, when nearest-neighbor mode coupling is dominant, then Dozier-Tappert's mode energy equation has a diffusion equation-like nature. As a result, the off-diagonal elements of the scattering matrix in the energy equation indicate the strength of nearest-neighbor mode coupling. It was then shown that modes that have their upper turning depths in the region of greatest sound speed perturbation experience the strongest mode coupling. The frequency dependence of mode coupling, in terms of mode coupling and attenuation ranges, and in the strength of mode coupling, showed that higher frequencies result in stronger mode coupling with coupling effects occurring over shorter ranges. These results are reiterated by the examination of mode energies which showed greater mode coupling at 1000 Hz than was observed by Colosi *et al.* (2012b) at 200 Hz to 400 Hz in a similar propagation environment. Lastly, the adiabatic phase randomization range was used to demonstrate the loss of mode coherence and it was observed that modes with turning depths in the thermocline exhibited large fluctuations in decorrelation range.

Overall, these results for mode energy, coherence, and mean intensity point the way toward greater use of transport theory to predict important acoustic observables such as mean and variance of acoustic intensity. The different coupling regimes at high frequency also necessitate a reanalysis of the effects of non-linear internal waves on mean intensity. Colosi *et al.* (2012b) found that when adiabatic effects result in a rapid phase randomization of acoustic modes, the impact of non-linear internal waves further along the propagation path has little effect on intensity moments. However, as we find that higher modes preserve their coherence at higher frequencies, they can now be expected to be more susceptible to phase randomization by nonlinear internal waves, at short ranges, before attenuation results in their being stripped from the water column. Thus, the effect of nonlinear internal waves on the acoustic moments at high frequencies remains an open research question.

Another phenomenon that can be important in shallow water, especially at high frequencies, is surface wave scattering. The canonical effects of surface waves on acoustic propagation have been well studied (McDaniel, 1993; Dahl, 2001), and include a transport theory for mode coupling by surface waves (Thorsos *et al.*, 2004, 2010). Work is currently under way to combine transport theories for surface and internal wave scattering effects in shallow water.

Limitations of the current model include an assumption of GM statistics for linear shallow water internal waves. While this assumption has been shown to be largely valid (Kim *et al.*, 2001; Raghukumar *et al.*, 2010), other sources of sound speed fluctuation such as spice can be important in shallow water (Colosi *et al.*, 2012a). The assumption of adiabatic phase variation, while shown to be valid in the somewhat weak mode coupling scenario studied here, can also be a limitation in the presence of stronger mode coupling. Increased mode coupling can be expected in the presence of larger sound speed perturbations caused by stronger internal wave activity, or over longer propagation distances. Finally, the edge effect correction was made using a GM-equivalent Lorentzian spectrum. While the result shows an excellent agreement with Monte Carlo simulations, a formal derivation specifically for the GM-spectrum would be desirable.

ACKNOWLEDGMENTS

This work is supported by the Office of Naval Research. K.R. is grateful to the National Academy of Sciences for support through the National Research Council research associateship program.

APPENDIX: DERIVATION OF SCATTERING MATRIX FOR INTERNAL WAVES

The internal wave scattering matrix is given by

$$I_{mn,qp} = \int_0^\infty d\xi \Delta_{mn,qp}(\xi) e^{-ik_{qp}\xi}, \tag{A1}$$

where $\Delta_{mn,qp}(\xi) = \langle \Gamma_{mn}(r)\Gamma_{qp}(r+\xi)\rangle$ is the correlation function of the symmetric mode coupling matrix [Eq. (3)] in the presence of internal waves, for range separation ξ. The acoustic mode wavenumber difference is $k_{qp} = k_p - k_q$. The correlation operation needed to calculate $\Delta_{mn,qp}(\xi)$ can be recast as an inverse Fourier transform of an isotropic wavenumber spectrum of sound speed perturbations, $S_j(k)$. This operation allowed Colosi *et al.* (2012b) to write the scattering matrix as

$$I_{mn,qp} = \sum_{j=1}^{J} G_{mn}(j) G_{qp}(j) \int_0^\infty dk \frac{S_j(k)}{\sqrt{k^2 - k_{qp}^2}}. \tag{A2}$$

Colosi *et al.* (2012b) evaluated the wavenumber integral in Eq. (A2) numerically. However, further examination of the expression for the scattering matrix [Eq. (A2)] in this paper allows for new closed-form expressions when $S_j(k)$ is parameterized by a GM spectrum,

$$S_j(k) = H(j)\frac{4}{\pi}\frac{k^2 k_j}{\left(k^2 + k_j^2\right)^2}. \tag{A3}$$

A numerically tractable expression for the scattering matrix can be sought by making trigonometric substitutions, following which the wavenumber integral can be expressed as

$$\int_0^\infty dk \frac{S_j(k)}{\sqrt{k^2-k_{qp}^2}} = H(j)\frac{4}{\pi}\frac{k_j}{k_{qp}^2}\left[\int_0^{\pi/2}\frac{\sin\theta}{(1+a^2\sin^2\theta)^2}d\theta + i\int_0^{\pi/2}\frac{\sin^2\theta}{(\sin^2\theta+a^2)^2}d\theta\right], \tag{A4}$$

where $a = k_j/|k_{qp}|$. Remarkably, the integrable singularity at $k = |k_{qp}|$ is now removed. For the special case of $k_{qp} = 0$, the integral has the form

$$\int_0^\infty dk \frac{S_j(k)}{k} = H(j)\frac{2}{\pi}\frac{1}{k_j}. \tag{A5}$$

The angular integrals, Eq. (A4), can be analytically solved to yield

$$\int_0^\infty dk \frac{S_j(k)}{\sqrt{k^2-k_{qp}^2}} = H(j)\frac{4a}{\pi|k_{qp}|}\left[\frac{1}{2(a^2+1)} + \frac{\operatorname{atanh}\left(\sqrt{\frac{a^2}{a^2+1}}\right)}{2a(a^2+1)^{3/2}} + i\frac{\pi}{4a(a^2+1)^{3/2}}\right]. \tag{A6}$$

In numerical calculations of the spatial coherence, the wavenumber integral must be truncated at a maximum wavenumber due to the inaccurate high-wavenumber roll-off characteristics of the WKB internal wave dispersion relation. The maximum wavenumber can be expressed as $k_{\max} = k_j\,(N_{\max}/f)$, where $N_{\max}$ is a maximum buoyancy frequency. The choice of $k_{\max}$ is not very important because $\langle I\rangle$ and $\langle I^2\rangle$ are not very sensitive to this cutoff. Quantities that are sensitive to $k_{\max}$ are the temporal and horizontal coherence (Colosi *et al.*, 2013). Nevertheless, Eq. (A4) needs to be rewritten as

$$\int_0^{k_{\max}} dk \frac{S_j(k)}{\sqrt{k^2-k_{qp}^2}} = H(j)\frac{4a}{\pi|k_{qp}|}\left[\int_{\theta_{\min}}^{\pi/2}\frac{\sin\theta}{(1+a^2\sin^2\theta)^2}d\theta + i\int_0^{\pi/2}\frac{\sin^2\theta}{(\sin^2\theta+a^2)^2}d\theta\right], \tag{A7}$$

where $\sin\theta_{\min} = |k_{qp}|/k_{\max}$. Fortunately, this integral can also be analytically solved to yield

$$\int_0^{k_{\max}} dk \frac{S_j(k)}{\sqrt{k^2-k_{qp}^2}} = H(j)\frac{4a}{\pi|k_{qp}|}\left[\frac{\cos\theta_{\min}}{(a^2+1)(a^2+2-a^2\cos 2\theta_{\min})} + \frac{\operatorname{atanh}\left(\sqrt{\frac{a^2}{a^2+1}}\cos\theta_{\min}\right)}{2a(a^2+1)^{3/2}} + i\frac{\pi}{4a(a^2+1)^{3/2}}\right]. \tag{A8}$$

For the special case of $k_{qp} = 0$,

$$\int_0^{k_{\max}} dk \frac{S_j(k)}{k} = H(j)\frac{2}{\pi}\frac{1}{k_j}\frac{k_{\max}^2}{k_{\max}^2+k_j^2}. \tag{A9}$$

[1]Equation (18) in Colosi *et al.* (2012b) contains a typo: A multiplicative factor of r is missing on the left-hand side.

Apel, J. R., Badiey, M., Chiu, C.-S., Finette, S., Headrick, R. H., Kemp, J., Lynch, J. F., Newhall, A. E., Orr, M. H., Pasewark, B. H., Tielbuerger, D., Turgut, A., von der Heydt, K., and Wolf, S. (**1997**). "An overview of the 1995 SWARM shallow-water internal wave acoustic scattering experiment," IEEE J. Oceanic Eng. **22**, 465–500.

Chandrayadula, T., Colosi, J. A., Dzieciuch, M. A., Worcester, P. F., Andrew, R. K., Mercer, J. A., and Howe, B. M. (**2013**). "Observations and transport theory analysis of low frequency, long range mode propagation in the Eastern North Pacific Ocean," J. Acoustic Soc. Am. **134**, 3144–3160.

Colosi, J. A., and Baggeroer, A. B. (**2004**). "On the kinematics of broadband multipath scintillation and the approach to saturation," J. Acoustic Soc. Am. **116**, 3515–3522.

Colosi, J. A., and Brown, M. G. (**1998**). "Efficient numerical simulations of stochastic internal wave induced sound speed perturbation fields," J. Acoustic Soc. Am. **103**, 2232–2235.

Colosi, J. A., Chandrayadula, T., Voronovich, A., and Ostashev, V. (**2013**). "Coupled mode transport theory for sound transmission through an ocean with random sound speed perturbations: Coherence in deep water environments," J. Acoustic Soc. Am. **134**, 3119–3133.

Colosi, J. A., Duda, T. F., Lin, Y.-T., Lynch, J. F., Newhall, A. E., and Cornuelle, B. D. (**2012a**). "Observations of sound-speed fluctuations on

the New Jersey continental shelf in the summer of 2006," J. Acoustic Soc. Am. **131**, 1733–1748.
Colosi, J. A., Duda, T. F., and Morozov, A. K. (**2012b**). "Statistics of low-frequency normal mode amplitudes in an ocean with random sound-speed perturbations: First and second moments of intensity in shallow-water environments," J. Acoustic Soc. Am. **131**, 1749–1761.
Colosi, J. A., and Morozov, A. K. (**2009**). "Statistics of normal-mode amplitudes in an ocean with random sound-speed perturbations: Cross coherence and mean intensity," J. Acoustic Soc. Am. **126**, 1026–1035.
Creamer, D. B. (**1996**). "Scintillating shallow water waveguides," J. Acoustic Soc. Am. **99**, 2825–2838.
Dahl, P. H. (**2001**). "High-frequency forward scattering from the sea surface: The characteristic scales of time and angle spreading," IEEE J. Oceanic Eng. **26**, 141–151.
Dozier, L. B. (**1982**). "A coupled-mode model for spatial coherence of bottom-interacting energy," in *Proceedings of the Stochastic Modeling Workshop*, edited by C. W. Spofford and J. M. Haynes (ARL-University of Texas, Austin, TX), pp. 28-1–28-46.
Dozier, L. B., and Tappert, F. D. (**1978a**). "Statistics of normal mode amplitudes in a random ocean. I. Theory," J. Acoustic Soc. Am. **63**, 353–365.
Dozier, L. B., and Tappert, F. D. (**1978b**). "Statistics of normal mode amplitudes in a random ocean. II. Computations," J. Acoustic Soc. Am. **64**, 533–547.
Flatte, S. M., Dashen, R., Munk, W. H., Watson, K. M., and Zachariasen, F. (**1979**). *Sound Transmission Through a Fluctuating Ocean* (Cambridge University Press, Cambridge), pp. 1–320.
Garrett, C., and Munk, W. H. (**1979**). "Internal waves in the ocean," Annu. Rev. Fluid Mech. **11**, 339–369.
Jensen, F. B., Kuperman, W. A., Porter, M. B., and Schmidt, H. (**1994**). *Computational Ocean Acoustics* (AIP, Woodbury, NY), Chap. 5.8.
Katsnelson, B., Petnikov, V., and Lynch, J. F. (**2012**). *Fundamentals of Shallow Water Acoustics* (Springer, New York), pp. 1–540.
Kim, S., Kuperman, W. A., Hodgkiss, W. S., Song, H. C., and Edelmann, G. F. (**2003**). "Robust time-reversal focusing in the ocean," J. Acoustic Soc. Am. **114**, 145–157.
Lynch, J. F., and Tang, D. (**2008**). "Overview of shallow water 2006 JASA EL Special Issue Papers," J. Acoust. Soc. Am. **124**, EL63–EL65.
McDaniel, S. T. (**1993**). "Sea surface reverberation: A review," J. Acoustic Soc. Am. **94**, 1905–1922.
Munk, W. H., Worcester, P. F., and Wunsch, C. (**1995**). *Ocean Acoustic Tomography* (Cambridge University Press, London), Chap. 5.
Raghukumar, K., Cornuelle, B. D., Hodgkiss, W. S., and Kuperman, W. A. (**2010**). "Experimental demonstration of pressure sensitivity kernels," J. Acoustic Soc. Am. **128**, 989–1003.
Tang, D., Moum, J. N., Lynch, J. F., Abbot, P., Chapman, R., Dahl, P. H., Duda, T. F., Gawarkiewicz, G., Glen, S., Goff, J. A., Graber, H., Kemp, J., Maffei, A., Nash, J. D., and Newhall, A. E. (**2007**). "Shallow water'06—A joint acoustic propagation/nonlinear internal wave physics experiment," Oceanography **20**, 156–167.
Thorsos, E. I., Henyey, F. S., Elam, W. T., Hefner, B. T., Reynolds, S. A., and Yang, J. (**2010**). "Transport theory for shallow water propagation with rough boundaries," AIP Conf. Proc. **1272**, 99–105.
Thorsos, E. I., Henyey, F. S., Elam, W. T., Reynolds, S. A., and Williams, K. L. (**2004**). "Modeling shallow water propagation with scattering from rough boundaries," AIP Conf. Proc. **728**, 132–140.